



Investigation of non-local screening in *K*-edge XANES for $\text{Pr}_{0.67}\text{Sr}_{0.33}\text{MnO}_3$ under high pressure

Bangmin Zhang^{a, b, c, 1}, Qiaoshi Zeng^{d, e, 1}, Ronghui Kou^{c, f}, Liuxiang Yang^e, Hongbo Lou^d, Steve M. Heald^c, Jingsheng Chen^a, Yang Ding^{d, *}, Cheng-Jun Sun^{c, **, ***}, Gan Moog Chow^{a, ***, **}

HPSTAR
751-2019



^a Department of Materials Science and Engineering, National University of Singapore, 117576, Singapore

^b School of Physics, Sun Yat-sen University, 510275, Guangzhou, China

^c Argonne National Laboratory, Advanced Photon Source, Argonne, IL 60439, USA

^d Center for High Pressure Science and Technology Advanced Research, Shanghai 201203, China

^e HPSynC, Geophysical Laboratory, Carnegie Institution of Washington, 9700 South Cass Avenue, Argonne, IL 60439, USA

^f Key Laboratory of Electromagnetic Processing of Materials (Ministry of Education), Northeastern University, Shenyang 110819, China

ARTICLE INFO

Article history:

Received 27 November 2018

Received in revised form

27 February 2019

Accepted 31 March 2019

Available online 4 April 2019

Keywords:

Electronic structure

High pressure

Manganite

XANES

Phase change

Crystal structure

ABSTRACT

The electronic excitation of 3d transition metal oxide depends on the hybridization between orbitals of different ions, and is related to the materials properties. In this work, we systematically study the effect of hydrostatic pressure up to ~20 GPa on the crystal structure and electronic structure of $\text{Pr}_{0.67}\text{Sr}_{0.33}\text{MnO}_3$ powder, using Mn *K*-edge X-ray absorption near edge structure and X-ray diffraction at room temperature. With the increase of pressure, the energy position of non-local screened feature moves towards feature without screening due to the enhanced transition energy; however, the intensity (probability) of non-local screened feature increases with the pressure. Further study suggests that the pressure-induced antiferromagnetic phase, affecting hybridization between neighboring Mn ions with spin sensitivity, increase the probability of non-local charge transfer and corresponding intensity of non-local screened feature. The spin-sensitivity of non-local screening may be a useful parameter for characterization of material properties.

© 2019 Published by Elsevier B.V.

1. Introduction

Electronic excitation of strongly-correlated-electron materials are affected by electron-electron interaction [1–3], which induces many interesting phenomena such as ferromagnetic phase transition in 3d transition metal compounds and high temperature superconductivity [4,5]. 3d transition metal compounds, including manganites, show some interesting properties such as high spin polarization and colossal magnetoresistance, and provide promising potential in spintronics devices. Much work has focused on the core-level x-ray photoemission of 3d transition metal oxide,

and the appearance of many-body satellites is well documented. Using hard X-ray photoemission spectroscopy (HAXPES), a well-screened peak at the lower binding energy side of Mn 2*p* main line in $\text{La}_{1-x}\text{Sr}_x\text{MnO}_3$ has been observed [6], which only appeared in magnetic-metallic phase and was attributed to the electronic configuration $2p^53d^5C$. The C represented an electron hole in coherent band around the Fermi level. Michel van Veenendaal [7] proposed that the well-screened peak comes from the non-local charge transfer between neighboring Mn (inter-site) ions rather than the charge transfer between Mn and O ions in the same MnO_6 octahedral, named as non-local screened feature, which is sensitive to ferromagnetic magnetic ordering. However, Ni 2*p* core-level spectrum of antiferromagnetic-insulator NiO also showed strong well-screened peak [8], which was attributed to the electronic configuration $2p^53d^5Z$ with screening from Zhang-Rice (ZR) doublet states around the Fermi level. The Z represented an electron hole in the ZR doublet states. In LaCoO_3 , similar well-screened feature at the lower binding energy existed [9] in the Co 2*p* HAXPES with spin-sensitivity to orbital occupancy, high spin configuration

* Corresponding author.

** Corresponding author.

*** Corresponding author.

E-mail addresses: yang.ding@hpstar.ac.cn (Y. Ding), cjsun@aps.anl.gov (C.-J. Sun), msecgm@nus.edu.sg (G.M. Chow).

¹ Equal contributions.

or low spin configuration. This well-screened feature seems to exist in different magnetic ordering system, but the properties of this feature are still under debate [10,11]. Further study of correlation between magnetic ordering and screened feature is necessary to clarify the argument. In addition, the inter-site charge transfer process in system with strongly correlated materials, such as TiO_2 and WO_3 , is important for its performance in electronic devices, solar cells and photoelectrochemistry [12–15]. Hence further study of screening in spectroscopy for strongly correlated system is necessary.

Strongly correlated manganite ($\text{Ln}_{1-x}\text{Sr}_x\text{MnO}_3$, Ln is the lanthanide family) has high spin polarization and colossal magnetoresistance effect [5]. And the materials properties are determined by the electronic structure, which depends on delicate balance between different interactions, including double-exchange (DE) and super-exchange (SE) interaction. In such system, the 3d orbitals of transition metal are more sensitive to the effect of correlation than the p orbitals [16]. Hence, most work focuses on the L-edge X-ray absorption due to the many-body nature of the electronic structure rather than the K-edge absorption. However, recent work showed that features measured in 2p Ni HAXPES, including local and non-local screened peaks, were also present in the Ni K-edge x-ray absorption spectroscopy (XAS) of NiO, and X-ray fluorescence spectroscopy has been proposed as a probe of charge transfer excitations [16,17]. The explanation of the dipolar K-edge XAS cross section usually is based on a standard single particle model, neglecting many-body effect presented in XPS. Previous theoretical work has shown that there is a close relationship [16] between XAS and XPS, described as the $I_{\text{XAS}}(t) = I_{\text{XPS}}(t) * I_0(t)$. Including the many-body effect with measured XPS, the measured XAS could be well reproduced through above relationship. In addition, the many-body effect in $I_0(t)$ may further contribute to the detailed features of XAS. These suggest that studying the K-edge XAS of manganite could understand many-body effects further and shed light on other strongly correlated systems.

With similarity between 3d transition metal oxides, Mn K-edge XAS of manganite may provide useful information on the excited electronic structure. For example, previous study showed that the detailed shape of Mn K-edge X-ray absorption near edge structure (XANES) depends on the electronic configurations with/without charge transfer between Mn and O in the same MnO_6 octahedral [18]. The corresponding energy separation depends on the value of several parameters [6–9], such as the d-d Coulomb interaction U , the charge transfer energy Δ and the hybridization t . Since all these parameters are sensitive to crystal structure, it would be an effective way to study the electronic structure of correlated system by modulating the crystal structure under high pressure. In this work, we systematically study the effect of hydrostatic pressure up to ~20 GPa on the crystal structure and electronic structure of $\text{Pr}_{0.67}\text{Sr}_{0.33}\text{MnO}_3$ (PSMO) powder, combining Mn K-edge XANES and X-ray diffraction at room temperature. With the increase of pressure, the energy position of screened feature moves towards non-screened feature due to the enhanced transition energy, resulting in decreased energy difference (δE_{ns-s}) between these features. However, the intensity (probability, P_s) of the non-local screened feature increases with pressure. It is found that the pressure-induced antiferromagnetic magnetic phase affects the hybridization between different Mn ions as well as the intensity of non-local screened feature.

2. Experimental details

The PSMO powder was obtained by sintering of mixed Pr_6O_{11} , Mn_3O_4 , and SrCO_3 precursor powders. The sintered powder was

measured using X-ray diffraction for confirmation of formation of $\text{Pr}_{0.67}\text{Sr}_{0.33}\text{MnO}_3$, then pressed into a pellet. High-pressure experiments [19–21] were performed with the Mao-type panoramic diamond anvil cells, and the pressures were determined by ruby fluorescence. For the XAS experiment, we used a Mao-type panoramic diamond anvil cell (DAC) to generate high pressure. The anvil size was ~400 μm . Beryllium was used as the x-ray transparent gasket. The sample was mixed with silicone oil to obtain suitable sample thickness. Silicone oil also acted as the pressure transmitting medium. The sample chamber was a hole with a diameter of ~40 μm drilled in the pre-indented beryllium gasket. A tiny ruby ball was loaded near the hole center as the pressure calibrant. The pressure gradient was small (less than 0.04 GPa/ μm at 20 GPa) since the sample chamber was relatively small (10% of the anvil culet size). [22] X-ray beam went sideway through the beryllium gasket rather than two thick diamond anvils. [20] XANES measurements were performed using linear polarized X-rays at the undulator beamline 20-ID-B of the Advanced Photon Source (APS), Argonne National Laboratory, USA. The Si (111) monochromator with resolution $\delta E/E = 1.3 \times 10^{-4}$ was used. The vertical and horizontal slit sizes before the Kirkpatrick-Baez (KB) focusing mirrors were 300 μm and 460 μm , respectively. The full width at half-maximum (FWHM) of the focused x-ray beam was 6 μm in both horizontal and vertical directions. The XANES was collected in fluorescence mode using a 12-element Ge solid-state detector. The XANES normalization was conducted using Athena software with same normalization parameters for all curves; the interpolative smoothing method with three iterations was employed during data processing, which did not change the absorption curve noticeably, and the derivative curves were obtained from the smoothed XANES spectra. [18] Details on the beamline optics and instruments may be found elsewhere [23,24]. In-situ high pressure X-ray diffraction was measured at the beamline 12.2.2 at Advanced Light Source, Lawrence Berkeley National Laboratory, California, US. For the XRD experiment, the sample was loaded into a Mao-type symmetric DAC with the anvil culet size of ~400 μm . The sample chamber was a hole with a diameter of ~120 μm drilled in a pre-indented (~20 GPa) T301 stainless steel gasket. The pressure medium was silicone oil, and the x-ray beam size was 10 $\mu\text{m} \times 10 \mu\text{m}$. The pressure of the sample environment was determined by the fluorescence of a tiny ruby ball loaded near the center of sample chamber. X-ray was shining at the center near the ruby ball to minimize the difference between the measured pressure and the real pressure of the sample probed. The in-situ resistance of $\text{Pr}_{0.67}\text{Sr}_{0.33}\text{MnO}_3$ pellet under pressure was measured using a hand made four-probe-circuit in a Cross-DAC (anvil culet size: ~400 μm). More details of the measurement can be found in Ref. [25].

3. Results

This section first shows the trend of X-ray absorption as a function of pressure, and discusses the assignment of the peaks with XANES simulation. The results of X-ray diffraction are used to correlate the pressure-induced phase transition with the X-ray absorption. Fig. 1 shows the Mn K-edge XANES under different pressures. The main peak shifts to higher energy position with increasing pressure, which is consistent with the shortening of the Mn–O bond length [18] under pressure. Detailed analysis of 1st derivative of Mn K-edge XANES in Fig. 1(b), shows three distinct features. First, the position of B1 feature remains constant under different pressures; Second, B2 feature shifts to higher energy position with a slight decrease in intensity; Third, B3 feature shows the most interesting behavior of a large shift to higher energy position and an increase of intensity with increasing pressure, as summarized in Fig. 1(c). With increasing pressure, the B3 feature

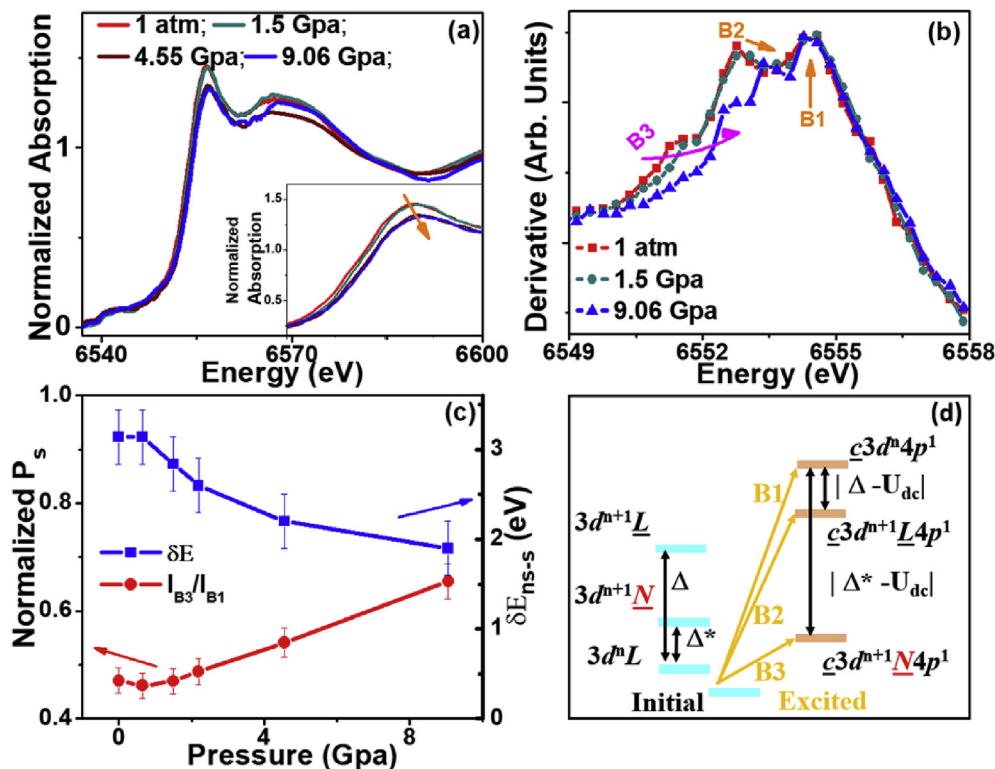


Fig. 1. (a) Mn K edge XANES and (b) corresponding 1st derivative for powder $\text{Pr}_{0.67}\text{Sr}_{0.33}\text{MnO}_3$ measured at different pressure ($T = 298\text{ K}$). The inset is the enlarged view around the peak position. Three features appears in the 1st derivative curve, and (c) shows the intensity of B3 feature (normalized to B1), and energy shift of B3 feature with respect to that at 1 atm. (d) The electronic configurations of initial and excited status. N , L , and c with underline represent a charge hole at neighboring sites, at local O ligand, and onsite Mn core orbital, respectively. Δ and Δ^* , V and V^* are charge transfer energy and hybridization between Mn $3d$ orbital and oxygen $2p$ orbital or non-local states, respectively. U_{dc} is the core-hole potential.

shifts by $\sim 1.1\text{ eV}$ towards the B1 feature, and the normalized intensity (taking B1 feature as reference) increases from ~ 0.46 to 0.62 . In order to understand the origin of these features, we measured Mn K -edge XANES for a 100 nm PSMO film deposited on (001) LaAlO_3 substrate at different temperatures. As shown in Fig. S1, the Mn K -edge XANES of PSMO film shows similar features, however the positions of B2 and B3 features do not change with decreasing temperature. In a large temperature range covering paramagnetic (PM) to ferromagnetic (FM) phase transition, B3 feature is temperature independent [26]. Hence, the pressure-dependent B3 feature in PSMO powder could not be attributed to the PM to FM transition, despite the hydrostatic pressure induced PM-to-FM phase transition [27,28] has been well studied.

Although the charge-transfer generally play only a small role in the final state of XAS compared to X-ray photoemission, the effects of charge-transfer occur in the ground state, and then the measured K -edge XAS spectrum would reflect these effects due to the additional core-hole potential. In PSMO, due to the hybridization between Mn $3d$ orbitals and O $2p$ orbitals there exists a mixture of O $2p$ orbitals on the Mn site. Previous study [18] showed that the initial electronic configuration with n electrons ($n = 4$ for Mn^{3+} site, and 3 for Mn^{4+} site) in Mn $3d$ orbitals may be described as a mixture of $3d^nL$ and $3d^{n+1}L$, and the excited configuration could be $c3d^nL4p^1$ and $c3d^{n+1}L4p^1$. L refers to the O ligands, c refers to a core hole at the excited (on-site) Mn site, and L refers to one hole in the O ligands resulting from the local charge transfer from the O $2p$ to empty Mn $3d$ orbitals in the same MnO_6 , named as local charge transfer. The B1 feature is attributed to the $c3d^nL4p^1$ configuration without charge transfer as shown in Fig. 1(d). The constant position of B1 feature in the current work is consistent with the conclusion

[29] that the Coulombic interaction does not change under the high pressure. In the $c3d^{n+1}L4p^1$ configuration, the Coulombic interaction between Mn $1s$ core hole and the extra $3d$ electron would lower the total energy. Then the B2 feature is attributed to configurations $c3d^{n+1}L4p^1$ with local charge transfer (local screened feature). As seen in Fig. 1(b), B2 and B3 features show different behaviors that suggest they should come from different physical processes.

Then the first principle simulation using FEFF8.4 code has been carried out to provide more information on B3 feature. The 118 atomic cluster was built based on XRD results (discussed later) and the simulation details are found elsewhere [30]. Fig. 2(a) shows the p , d -projected density of states (DOS) on the Mn site for bulk PSMO under different pressures, with the Fermi level set to zero. Normally the splitting of the p -DOS causes the multiple features in the K -edge XAS. Careful examination indicates that there is a wide peak in the p -DOS around 12 eV ; around the similar energy range, a 0.8 eV shift of the d -DOS to higher energy position occurs, shown as indigo and red curves in Fig. 2(a), close to the observed B3 feature shift 1.1 eV between absorption under 1 atm and 9.3 GPa . These results suggest that the d -DOS may hybridize with the p -DOS, affecting the absorption spectrum. Additional simulations for PSMO films on (001) SrTiO_3 (STO), (001) LaAlO_3 (LAO), and (110) NdGaO_3 (NGO) substrates with different lattice mismatch strain, do not have such shift of d -DOS around 12 eV , as shown in Fig. 2(b), which is consistent with experimental results that there is no shift of B3 feature [18]. Above discussion suggests that the shift of d -DOS under pressure may contribute to the observed B3 feature.

The features from the many-body effects in XPS may be present in K -edge XAS, including both the local and non-local screened

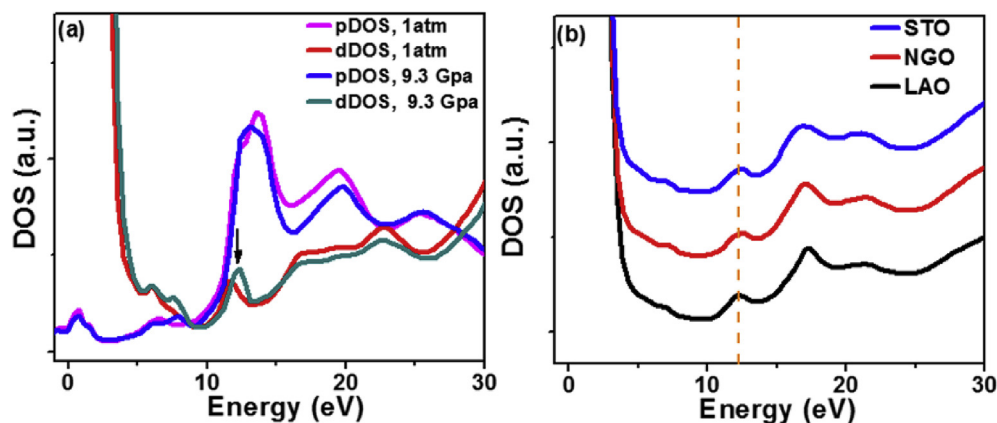


Fig. 2. (a) Simulated *p*- and *d*-projected DOS for PSMO under different pressure. The arrow indicates the shifting peak with pressure around 12 eV. (b) Similar *d*-projected DOS for 12-nm PSMO film on different substrate. There is no shift of for the 12 eV peak under different bi-axial strain.

features. Considering the difference of charge transfer energy (Δ) and hybridization (V) for different channels of charge transfer (local and non-local), the local screened and non-local screened states should be at different positions. The non-local screening is the charge screening from a neighboring MnO_6 unit to the core-excited Mn site due to the many-body effects in strongly correlated system, which would lower the energy of corresponding electronic configuration. Mn 2*p* XPS [6] indicates that the non-local screened peak is at lower binding energy, and $\Delta = 4.5$ eV for local screening and $\Delta^* \sim 0.5$ eV for non-local screening [6] are appropriately evaluated values under 1 atm. Hence for initial state the non-local charge transfer configurations $3d^{n+1}N$ (N indicates one hole in the neighboring Mn orbital) is at lower energy position compared to that with local charge transfer configurations $3d^{n+1}L$, and both are at higher energy position than $3d^n$ configuration. For the excited states, previous simulation has revealed that the configurations with charge transfer could be at lower energy positions, depending on the relative value [31] of charge transfer energy (Δ and Δ^*), core hole-*d* electron Coulombic attraction (U_{dc}) and *d*-*d* Coulombic interaction (U). According to the proposed value [6], $U_{dc} = 5.4$ eV and $U = 5.1$ eV, and the energy levels are illustrated in Fig. 1(d). The estimated energy difference between B2 and B1 feature is 0.9 eV, close to the experiment value 1.5 eV observed at 1 atm (step size is 0.3 eV during measurement); while the estimated energy difference between B3 and B1 peak is ~ 4.9 eV, which is higher than the experimental value 3.1 eV at 1 atm. The discrepancy between the estimation and experiment may come from the uncertainty of the Δ^* and U_{dc} in this particular system. The lack of information of these parameters under high pressure does not allow for a comparison of the experimental and estimated results at different pressure. The non-local screened features have been revealed in other 3*d* transition metal oxide, such as NiO [8] and $\text{V}_{1.98}\text{Cr}_{0.02}\text{O}_3$ [32], and similar energy level diagram has been proposed to explain the observed features [32–34]. Then the B3 feature is attributed to the non-local screened configurations $3d^{n+1}N4p^1$. For the *K*-edge XAS, theoretical simulation needs to consider the excitations in a large energy window above the Fermi level [35], and the full cluster model calculations with hybridization among the different electronic configurations warrants further study in future.

Then the trend of B2 and B3 features' position under pressure may be understood as below: The strength of screening [29] depends on two ingredients: the transition energies and the overlap integral of the two wave functions. Previous simulations on NiO and MnO in octahedral structure indicate that with applied pressure [34,36], the enhancement of transition energy dominates, which

would weaken the strength of screening with pressure, revealed as decreased energy difference between non-screened and screened features, δE_{ns-s} . Hence the overall effect of lowering the energy by core hole-electron interaction decreases, and then the absorption position of screened configurations (B2 and B3) approaches to the $3d^n L4p^1$ configurations (B1) without screening. With the enhancement of transition energy, the probability of charge transfer is supposed to decrease, which fits well with the trend of B2 feature. However, the intensity of B3 (probability of non-local screening) increases in current work (Fig. 1(b)), which cannot be explained by the enhancement of transition energy alone.

Considering the coupling between crystal structure and electronic structure, the crystal structure was studied at different pressures, as summarized in Fig. 3. Data analysis [19] was performed using GSAS (see Fig. S2). The discrepancy between the refinement and measured peaks may come from the limited pressure gradient and cation segregation [37]. All data analysis was carried out under the same process, and the discrepancy between the refinement and experiment should not affect the trend of lattice constant. Fig. 3(a) shows several XRD curves under different pressures. Some peaks, such as (111), disappear gradually with increasing pressure, indicating structural phase transition occurs. Fig. 3(b) shows the lattice constant and unit-cell volume normalized to that at 1 atm, and no discontinuity is observed in the pressure-volume curve. With the applied pressure, all normalized values show monotonous decrease, and detailed analysis is shown in Fig. 4(a). The lattice strain shows a crossover around 5.5 GPa, suggesting an orbital-ordered antiferromagnetic (AFM) phase with structural phase transition as reported in similar systems [19,38]. In manganite magnetic coupling depends on the electronic configurations. Both the antiferromagnetic SE between the core t_{2g} electrons and ferromagnetic DE through the itinerant e_g electrons exist, and the final spin arrangement depends on the delicate balance between them. According to the theory of crystal field, the 3*d* orbital of Mn would be split into triple degenerate t_{2g} and double degenerate e_g orbital by cubic crystal field, with t_{2g} located at lower energy level. Further tetragonal distortion of crystal structure would lift the degeneracy of the t_{2g} and e_g orbitals, and affects the electron occupancy accordingly. For both Mn^{3+} ($n = 4$) and Mn^{4+} ($n = 3$) site, 3 electrons occupy the t_{2g} spin-up orbitals, and the rest 1 electron on Mn^{3+} site would occupy the e_g spin-up orbitals, either $3d_{x-y}^{22}$ or $3d_{3z-z}^{22}$ depending on the structural distortion. With the applied pressure, the enhanced compression along the *b* axis (normal to MnO_2 planes) lifts the degeneracy of two e_g orbitals, and the $3d_{x-y}^{22}$ is favored for occupancy in current case. The favored $3d_{x-y}^{22}$

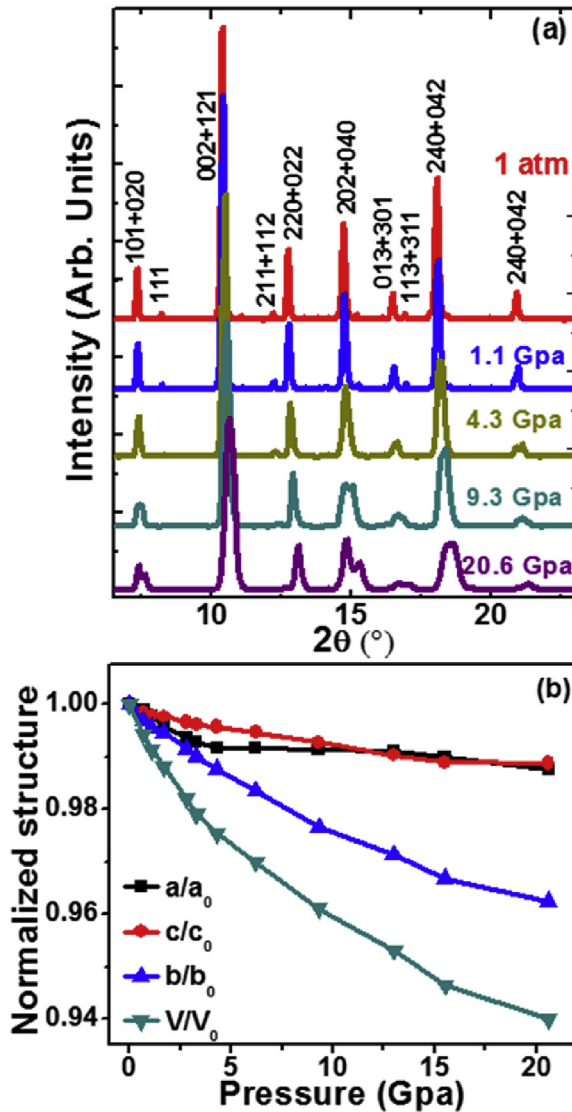


Fig. 3. (a) The X-ray powder diffraction patterns of bulk $\text{Pr}_{0.67}\text{Sr}_{0.33}\text{MnO}_3$ at various pressures ($T = 298\text{ K}$). The x-ray wavelength is 0.4959 \AA . (b) The calculated lattice constant and volume at different pressure with space group $Pnma$. The lattice constant and volume of unit cell is normalized to that at 1 atm (a_0, b_0, c_0, V_0).

orbital favors ferromagnetic (FM) DE in the MnO_2 plane, and the lack of $3d_{3z^2}$ electrons renders the antiferromagnetic SE dominant along the direction normal to the MnO_2 plane.

4. Discussion

This section first summarizes the pressure-induced phase transition. Then the effects of magnetic ordering, FM and AFM phase, on the non-local charge screening process are discussed. At the end the trend of the non-local feature is discussed for the entire range of pressure. Theoretical calculations predicts a critical splitting energy of two e_g orbitals 0.15 eV to trigger a phase transition [39]. According to the strain dependence on pressure below 5.5 GPa , the calculated pressure to trigger a phase transition is $\sim 1\text{ GPa}$. In addition, strain may induce the PM-FM phase transition, described in a phenomenological equation proposed by A. J. Millis [40,41], i.e. $T = T_0 \left(1 - \alpha \varepsilon_B - \frac{1}{2} \Delta \varepsilon_{JT}^2 \right) \sim T_0 (1 - \alpha \varepsilon_B) = T_0 (1 - \alpha P/K)$. Here ε_B is the bulk strain, ε_{JT} is the Jahn-Teller distortion, P is

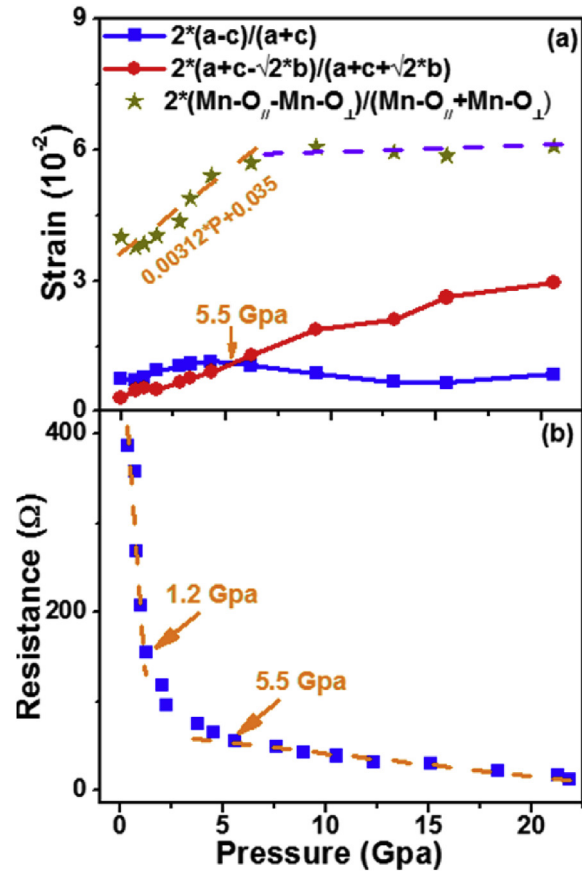


Fig. 4. The (a) strain for lattice and MnO_6 octahedral, and (b) resistance dependence on pressure (For $Pnma, b > a > c$). The orange dashed line is an estimated pressure dependence of strain, equal to $0.00312 \cdot P + 0.035$. Mn-O_{\parallel} and Mn-O_{\perp} represent the averaged bond length within and perpendicular to the ac plane, respectively. (For interpretation of the references to colour in this figure legend, the reader is referred to the Web version of this article.)

applied pressure, and Curie temperature at 1 atm $T_0 \sim 280\text{ K}$, [42] bulk modulus $K \sim 152\text{ GPa}$ [43] and $\alpha \sim 10$ [44] are estimated for $\text{Pr}_{0.67}\text{Sr}_{0.33}\text{MnO}_3$. Coincidentally, the required pressure for PM-FM transition at room temperature (300 K) is $\sim 1.1\text{ GPa}$, which is close to that triggering the AFM phase transition by lifting the degeneracy of two e_g orbitals. With further increase of pressure, the AFM and FM phase coexist, and the growth of AFM at the expense of the FM phase completes at 5.5 GPa , then the FM phase disappears. The atomic distance decreases with the increase of pressure from experimental results. The enhancement of transition energy dominates [29] the charge transfer process, and the structural change itself is not enough to explain the trend of B3 (increase of intensity with increasing pressure). Either the enhancement of Jahn-Teller distortion or the increase of local charge transfer from Mn-O hybridization could cause the decrease of intensity [45] of Mn K edge white line. The intensity of local charge transfer (Jahn-Teller distortion) decreases (increases) with increasing pressure from experimental results, and then the Jahn-Teller distortion should be responsible for the change of white line intensity rather than the Mn-O hybridization. Due to the correlation between the Jahn-Teller distortion and the FM-AFM transition, the drastic difference of white line intensity between low pressure and high pressure in Fig. 1(a) should correlate with the FM-AFM transition.

In this system, the transport properties highly depend on crystal structure, which shows similar characteristics and support above arguments: Below 1 GPa and above 5.5 GPa , it shows linear

dependence with pressure, and in the range $1 \text{ GPa} < P < 5.5 \text{ GPa}$ it is nonlinear. The resistivity decreases with the increasing pressure in the entire pressure range. At low pressure range $P < 1.2 \text{ GPa}$ with coexistence of FM and PM. The conductivity in FM manganite comes from the electron hopping between Mn ions, which would increase with increasing orbital overlapping, and shows fast decrease of resistivity with pressure. At high pressure $P > 5 \text{ GPa}$ in AFM phase, the conductivity changes quite slowly with pressure, which might be due to that at AFM phase the conductivity is controlled by thermal activation. [46] The detailed correlation between the behavior of resistivity and phase transition (XANES spectrum) needs further investigation. From above discussion, it is proposed that the PSMO experiences phase transitions with application of pressure, as shown in Fig. 5(a–c). At low pressure

$\sim 1 \text{ GPa}$, the PSMO experiences PM-FM phase transition, at the same time the AFM ordering phase is triggered; with further increase of pressure around 5.5 GPa , the FM-AFM phase transition completes. These magnetic/orbital ordering has effects on the electronic excitation as discussed below.

Non-local screening is sensitive to the orbital and magnetic ordering according to the previous work [7]. It is the orbital hybridization between the $3d$ orbital of excited (on-site) Mn site and the neighboring Mn sites that determines the probability of charge transfer, which depends on the arrangement of electronic structure and spin coupling as discussed below. In the FM phase without orbital ordering, the orbital occupancy of two neighboring Mn sites are illustrated in Fig. 5(d). Note that the on-site Mn ion should interact with the rest of environment (bands) rather than a single

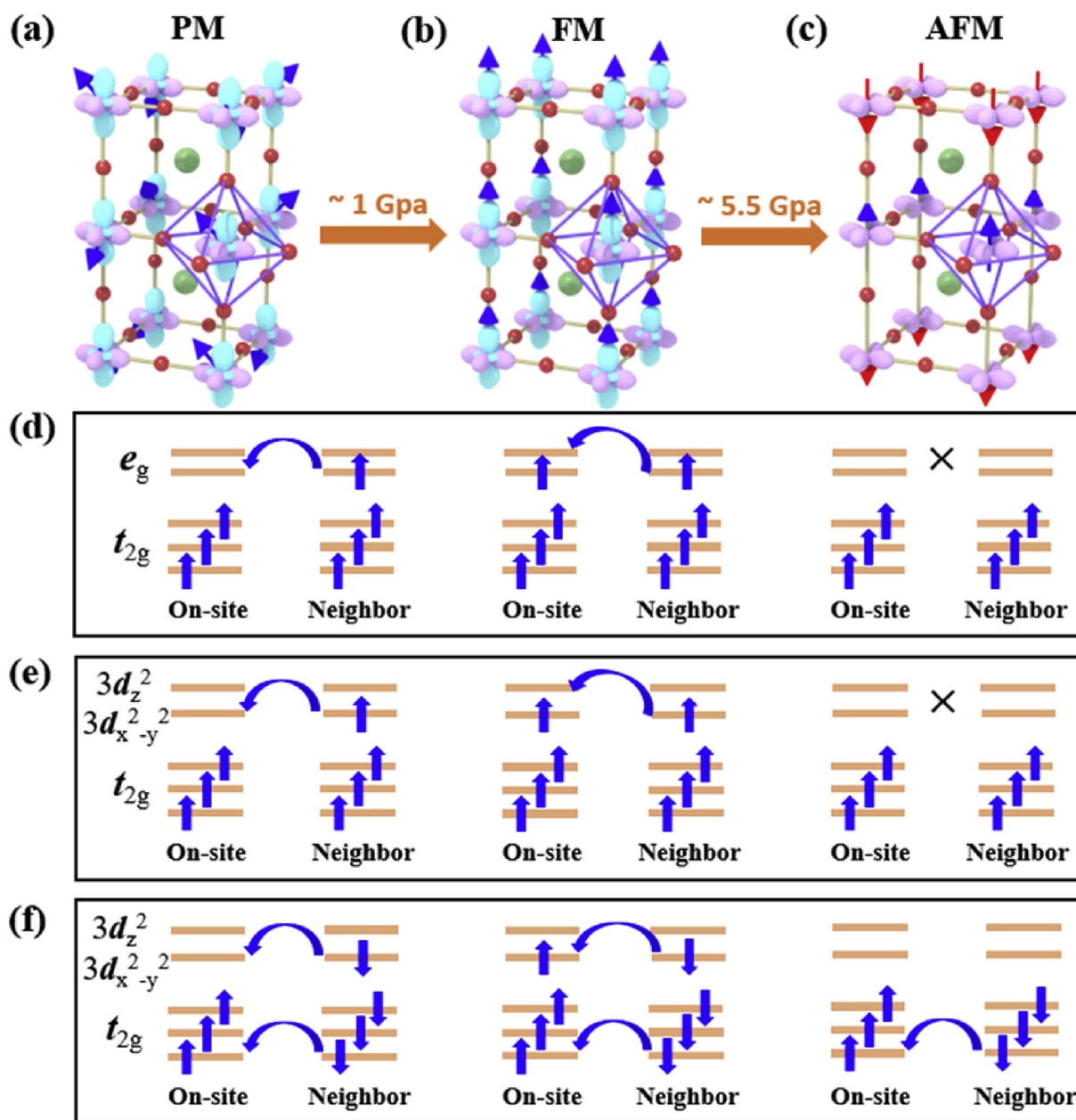


Fig. 5. Schematic depiction of orbital and magnetic ordering in (a) PM, (b) FM, and (c) AFM state. Mn^{3+} site has four $3d$ electrons, and Mn^{4+} site has three $3d$ electrons. Schematic depiction of non-local charge screening process between two Mn sites at (d) FM phase, (e) in the same MnO_2 plane with FM coupled ions and (f) at two MnO_2 neighboring plane with AFM coupled ions in the AFM phase. In (f), the neighboring spin-down electron would occupy the empty spin-down orbital of on-site Mn ion after charge transfer.

neighboring Mn site (discrete energy levels), and the rest of environment here is represented by the electronic arrangement of one particular Mn site for clarity in Fig. 5(d)–5(f). According to the DE mode, two neighboring Mn ions with different valences Mn^{3+} ($n = 4$) and Mn^{4+} ($n = 3$), could facilitate the exchange interaction, otherwise the DE interaction would be depressed. Similar trend occurs in the non-local screening process. For ions with different valences Mn^{3+} and Mn^{4+} , shown in the left of Fig. 5(d), the non-local screening could occur with charge transfer from neighboring $\text{Mn}^{3+} e_g$ orbital to the empty $3d e_g$ orbital of on-site Mn^{4+} ion. For two Mn^{3+} ions, shown in the center of Fig. 5(d), the electron through non-local charge transfer has to occupy the higher empty e_g orbital of on-site Mn^{3+} ion, which would decrease the probability of non-local charge transfer compared to the case in the left of Fig. 5(d). For two Mn^{4+} ions, shown in the right of Fig. 5(d), the non-local screening does not happen because of the empty e_g orbital, and the non-local screening through charge transfer from neighboring $\text{Mn}^{4+} t_{2g}$ to the on-site $\text{Mn}^{4+} e_g$ orbital is limited due to the symmetry mismatch of these orbital [9]. From neighboring Mn^{4+} to the on-site Mn^{3+} , the charge transfer process is similar as two Mn^{4+} ions in the right of Fig. 5(d), due to the empty e_g orbital at neighboring Mn^{4+} site, which is not shown in figure.

In the AFM phase, the spin of Mn ions located at the same MnO_2 plane is FM coupled, while spin of Mn ions located at two neighboring MnO_2 planes are AFM coupled, as illustrated in Fig. 5(c). For two Mn ions at the same MnO_2 plane, the situations in Fig. 5(e) are quite similar to that of the FM phase in Fig. 5(d). For two Mn ions at two neighboring MnO_2 planes with AFM coupling, it has several different situations in Fig. 5(f). The hybridization between the AFM spin moments is important for the non-local screening [47,48]. For ions with different valences Mn^{3+} and Mn^{4+} , shown in the left of Fig. 5(f), the non-local screening could occur with charge transfer through t_{2g} orbitals, and from neighboring $\text{Mn}^{3+} 3d_{x^2-y^2}$ to on-site $\text{Mn}^{4+} 3d_{3z^2}$ orbital with limited intensity due to the spatial separation of these two e_g orbitals. Here the on-site Mn ion has spin-up moment, and neighboring Mn ion has spin-down moment. Without consideration of spin-flip, after charge transfer the electron from neighboring Mn ion would occupy the spin-down orbital of the on-site Mn ion. For two Mn^{3+} ions, shown in the center of Fig. 5(f), the non-local screening could occur through t_{2g} orbitals, and e_g orbital with limited intensity due to the spatial separation of two e_g orbitals. For two Mn^{4+} ions, shown in the right of Fig. 5(f), the non-local screening does not occur through the empty e_g orbital, but it could occur through the t_{2g} orbitals. Note that the local screening through oxygen $2p$ and Mn $3d e_g$ orbitals always exists [9], and shows no dependence on the spin configuration.

Based on the above considerations, the gradual increase of the intensity of B3 feature with pressure may be understood as follow: In the FM phase, the pressure enhances the DE interaction, and the spins of neighboring Mn sites align parallel. In this case, the hybridization between on-site Mn $3d$ orbital and the neighboring Mn sites depends on the angle of spins [38], and the probability of hopping is proportional to $\cos \theta_{ij}/2$, where $\theta_{ij}/2$ is the angle between the t_{2g} core spins on neighboring sites i and j : parallel coupling would enhance the probability of charge transfer. Compared to the PM phase at 1 atm, the probability is enhanced due to the parallel arrangement of Mn spins in the framework of the DE model, which is consistent with previous study [6] showing that the ferromagnetic-metallic phase enhances the non-local screening. As shown in Fig. 1(c), there is a slow change of B3 intensity after 1 GPa. With further increase of pressure, the AFM phase dominates, and the SE interaction is enhanced faster than the DE interaction. The hybridization between the AFM spins contributes to the non-local screening. In addition, compared to FM phase, the additional non-local charge transfer through t_{2g} orbitals between AFM

coupled spins contributes to the non-local screening, as shown in Fig. 5(f). Then the enhanced SE in AFM phase causes a quick increase of B3 feature as shown in Fig. 1(c). With applied pressure, non-local screening is sensitive to the spin arrangement and the intensity of magnetic interactions.

5. Conclusions

In this work, we present a study of the electronic structure of PSMO under different pressures using X-ray absorption spectrum and X-ray diffraction. With the increase of pressure, the energy position of non-local screened features move towards feature without screening due to the enhanced transition energy, resulting in decreased energy difference between these features. However, the probability of non-local screening increases with increasing pressure. The pressure-induced magnetic phase transition affects the hybridization between on-site Mn $3d$ orbital and the neighboring Mn sites, determining the probability of non-local screening. This work demonstrate that the Mn– K edge may be used to detect the electronic structure in strongly correlated electron system, and the spin-sensitivity of the non-local screening may be useful to understand materials properties.

Conflicts of interest

There are no conflicts to declare.

Acknowledgements

The research was supported by the Singapore Ministry of Education Academic Research Fund Tier 2 under the Project No. MOE2015-T2-1-016 and the project No. MOE2018-T2-1-019, the Singapore Ministry of Education MOE T1 R-284-000-196-114, and the Singapore National Research Foundation under CRP Award No. NRF-CRP10-2012-02. Q.S.Z. thanks the support from the National Thousand Youth Talents Program in China. Sector 20 facilities at the Advanced Photon Source, and research at these facilities, are supported by the U.S. Department of Energy - Basic Energy Sciences, the Canadian Light Source and its funding partners, the University of Washington, and the Advanced Photon Source. Use of the Advanced Photon Source, an Office of Science User Facility operated for the U.S. Department of Energy (DOE) Office of Science by Argonne National Laboratory, was supported by the U.S. DOE under Contract No. DE-AC02-06CH11357. The XRD experiment was carried out at the beamline 12.2.2, Advanced Light Source (ALS). ALS is supported by the Director, Office of Science, DOE-BES under Contract No. DE-AC02-05CH11231.

Appendix A. Supplementary data

Supplementary data to this article can be found online at <https://doi.org/10.1016/j.jallcom.2019.03.415>.

References

- [1] N. Mannella, A. Rosenhahn, C.H. Booth, S. Marchesini, B.S. Mun, S.H. Yang, K. Ibrahim, Y. Tomioka, C.S. Fadley, Phys. Rev. Lett. 92 (2004) 166401.
- [2] N. Takubo, I. Onishi, K. Takubo, T. Mizokawa, K. Miyano, Phys. Rev. Lett. 101 (2008) 177403.
- [3] J. Zhang, X. Tan, M. Liu, S.W. Teitelbaum, K.W. Post, F. Jin, K.A. Nelson, D.N. Basov, W. Wu, R.D. Averitt, Nat. Mater. 15 (2016) 956–960.
- [4] M.S. Kim, J.B. Yang, Q. Cai, X.D. Zhou, W.J. James, W.B. Yelon, P.E. Parris, D. Buddhikot, S.K. Malik, Phys. Rev. B 71 (2005), 014433.
- [5] Elbio Dagotto, Takashi Hotta, A. Moreo, Phys. Rep. 344 (2001) 1.
- [6] K. Horiba, M. Taguchi, A. Chainani, Y. Takata, E. Ikenaga, D. Miwa, Y. Nishino, K. Tamasaku, M. Awaji, A. Takeuchi, M. Yabashi, H. Namatame, M. Taniguchi, H. Kumigashira, M. Oshima, M. Lippmaa, M. Kawasaki, H. Koinuma, K. Kobayashi, T. Ishikawa, S. Shin, Phys. Rev. Lett. 93 (2004) 236401.

- [7] M. van Veenendaal, *Phys. Rev. B* 74 (2006), 085118.
- [8] M. Taguchi, M. Matsunami, Y. Ishida, R. Eguchi, A. Chainani, Y. Takata, M. Yabashi, K. Tamasaku, Y. Nishino, T. Ishikawa, Y. Senba, H. Ohashi, S. Shin, *Phys. Rev. Lett.* 100 (2008) 206401.
- [9] A. Hariki, A. Yamanaka, T. Uozumi, *J. Phys. Soc. Jpn.* 84 (2015), 073706.
- [10] R.J.O. Mossaneck, I. Preda, M. Abbate, J. Rubio-Zuazo, G.R. Castro, A. Vollmer, A. Gutiérrez, L. Soriano, *Chem. Phys. Lett.* 501 (2011) 437.
- [11] C.Y. Kuo, T. Haupricht, J. Weinen, H. Wu, K.D. Tsuei, M.W. Haverkort, A. Tanaka, L.H. Tjeng, *Eur. Phys. J. Spec. Top.* 226 (2017) 2445–2456.
- [12] P. Li, X. Wang, H. Li, X. Yang, X. Zhang, L. Zhang, Y. Ozaki, B. Liu, B. Zhao, *Chem. Commun. (Camb)* 54 (2018) 6280–6283.
- [13] L.C. Wu, M.B. Nielsen, M. Bremholm, S.R. Madsen, J. Overgaard, M. Newville, Y.S. Chen, B.B. Iversen, *Chem. Commun. (Camb)* 51 (2015) 8868–8871.
- [14] V. Cristino, S. Marinello, A. Molinari, S. Caramori, S. Carli, R. Boaretto, R. Argazzi, L. Meda, C.A. Bignozzi, *J. Mater. Chem.* 4 (2016) 2995–3006.
- [15] Z. Zheng, N.R. Tummala, Y.T. Fu, V. Coropceanu, J.L. Bredas, *ACS Appl. Mater. Interfaces* 9 (2017) 18095–18102.
- [16] M. Calandra, J.P. Rueff, C. Gougoussis, D. Céolin, M. Gorgoi, S. Benedetti, P. Torelli, A. Shukla, D. Chandross, C. Brouder, *Phys. Rev. B* 86 (2012) 165102.
- [17] C. Gougoussis, M. Calandra, A. Seitsonen, C. Brouder, A. Shukla, F. Mauri, *Phys. Rev. B* 79 (2009), 045118.
- [18] B. Zhang, C.-J. Sun, P. Yang, W. Lu, B.L. Fisher, T. Venkatesan, S.M. Heald, J.-S. Chen, G.M. Chow, *Phys. Rev. B* 89 (2014) 195140.
- [19] Y. Ding, D. Haskel, Y.C. Tseng, E. Kaneshita, M. van Veenendaal, J.F. Mitchell, S.V. Sinogeikin, V. Prakapenka, H.K. Mao, *Phys. Rev. Lett.* 102 (2009) 237201.
- [20] Q.S. Zeng, Y. Ding, W.L. Mao, W. Yang, S.V. Sinogeikin, J. Shu, H.K. Mao, J.Z. Jiang, *Phys. Rev. Lett.* 104 (2010) 105702.
- [21] M. Baldini, V.V. Struzhkin, A.F. Goncharov, P. Postorino, W.L. Mao, *Phys. Rev. Lett.* 106 (2011), 066402.
- [22] F. Zhang, H. Lou, S. Chen, X. Chen, Z. Zeng, J. Yan, W. Zhao, Y. Wu, Z. Lu, Q. Zeng, *J. Appl. Phys.* 124 (2018) 115901.
- [23] S.M. Heald, J.O. Cross, D.L. Brewster, R.A. Gordon, *Nucl. Instrum. Methods Phys. Res. Sect. A Accel. Spectrom. Detect. Assoc. Equip.* 582 (2007) 215–217.
- [24] C.-J. Sun, D. Xu, S.M. Heald, J. Chen, G.-M. Chow, *Phys. Rev. B* 84 (2011), 140408(R).
- [25] Q.S. Zeng, V.V. Struzhkin, Y.Z. Fang, C.X. Gao, H.B. Luo, X.D. Wang, C. Lathe, W.L. Mao, F.M. Wu, H.K. Mao, J.Z. Jiang, *Phys. Rev. B* 82 (2010), 054111.
- [26] B. Zhang, C.-J. Sun, J.-S. Chen, T. Venkatesan, S.M. Heald, G. Moog Chow, *J. Appl. Phys.* 115 (2014) 17E116.
- [27] Y. Ding, C.C. Chen, Q. Zeng, H.S. Kim, M.J. Han, M. Balasubramanian, R. Gordon, F. Li, L. Bai, D. Popov, S.M. Heald, T. Gog, H.K. Mao, M. van Veenendaal, *Phys. Rev. Lett.* 112 (2014), 056401.
- [28] M. Sherafati, M. Baldini, L. Malavasi, S. Satpathy, *Phys. Rev. B* 93 (2016), 024107.
- [29] S.K. Panda, H. Jiang, S. Biermann, *Phys. Rev. B* 96 (2017), 045137.
- [30] G.E. Sterbinsky, P.J. Ryan, J.W. Kim, E. Karapetrova, J.X. Ma, J. Shi, J.C. Woicik, *Phys. Rev. B* 85 (2012), 020403(R).
- [31] J. Zaanen, C. Westra, G.A. Sawatzky, *Phys. Rev. B* 33 (1986) 8060–8073.
- [32] M. Taguchi, A. Chainani, N. Kamakura, K. Horiba, Y. Takata, M. Yabashi, K. Tamasaku, Y. Nishino, D. Miwa, T. Ishikawa, S. Shin, E. Ikenaga, T. Yokoya, K. Kobayashi, T. Mochiku, K. Hirata, K. Motoya, *Phys. Rev. B* 71 (2005) 155102.
- [33] A. Fujimori, F. Minami, *Phys. Rev. B* 30 (1984) 957–971.
- [34] S.M. Butorin, D.C. Mancini, J.-H. Guo, N. Wassdahl, J. Nordgren, M. Nakazawa, S. Tanaka, T. Uozumi, A. Kotani, Y. Ma, K.E. Myano, B.A. Karlin, D.K. Shuh, *Phys. Rev. Lett.* 77 (1996) 754.
- [35] P. Ravindran, A. Kjekshus, H. Fjellvåg, A. Delin, O. Eriksson, *Phys. Rev. B* 65 (2002).
- [36] J.M. Tomczak, T. Miyake, F. Aryasetiawan, *Phys. Rev. B* 81 (2010) 115116.
- [37] W. Lee, B. Yildiz, *ECS Trans.* 57 (2013) 2115–2123.
- [38] M. Baldini, Y. Ding, S. Wang, Y. Lin, C.A. Tulk, A.M. dos Santos, J.F. Mitchell, D. Haskel, W.L. Mao, *Phys. Rev. B* 86 (2012), 094407.
- [39] L. Abad, V. Laukhin, S. Valencia, A. Gaup, W. Gudat, L. Balcells, B. Martínez, *Adv. Funct. Mater.* 17 (2007) 3918–3925.
- [40] A.J. Millis, T. Darling, A. Migliori, *J. Appl. Phys.* 83 (1998) 1588.
- [41] H.S. Wang, E. Wertz, Y.F. Hu, Q. Li, D.G. Schlom, *J. Appl. Phys.* 87 (2000) 7409–7414.
- [42] C. Martin, A. Maignan, M. Hervieu, B. Raveau, *Phys. Rev. B* 60 (1999) 12191.
- [43] A. Srivastava, N.K. Gaur, *J. Phys. Conf. Ser.* 215 (2010), 012140.
- [44] Q. Li, H.S. Wang, Y.F. Hu, E. Wertz, *J. Appl. Phys.* 87 (2000) 5573–5575.
- [45] J.M. Chen, S.C. Haw, J.M. Lee, S.A. Chen, K.T. Lu, S.W. Chen, M.J. Deng, Y.F. Liao, J.M. Lin, B.H. Chen, F.C. Chou, N. Hiraoka, H. Ishii, K.D. Tsuei, E. Huang, *Phys. Rev. B* 86 (2012), 045103.
- [46] J.M.D. Coey, M. Viret, S.V. Molnan, *Adv. Phys.* 48 (1999) 167.
- [47] K. Okada, Y. Takeuchi, *J. Phys. Soc. Jpn.* 86 (2017), 064701.
- [48] A. Hariki, Y. Ichinozuka, T. Uozumi, *J. Phys. Soc. Jpn.* 82 (2013), 043710.